# An investigation into patient-specific 3D printed titanium stents and the use of etching to overcome Selective Laser Melting design constraints

McGee, Orla M.; Geraghty, Sam; Hughes, Celia; Jamshidi, Parastoo; Kenny, Damien P.; Attallah, Moataz M.; Lally, Caitríona

*DOI:*
10.1016/j.jmbbm.2022.105388



*Document Version*
Publisher's PDF, also known as Version of record

*Citation for published version (Harvard):*
McGee, OM, Geraghty, S, Hughes, C, Jamshidi, P, Kenny, DP, Attallah, MM & Lally, C 2022, 'An investigation into patient-specific 3D printed titanium stents and the use of etching to overcome Selective Laser Melting design constraints', *Journal of the Mechanical Behavior of Biomedical Materials*, vol. 134, 105388. https://doi.org/10.1016/j.jmbbm.2022.105388

journal of the mechanical behavior of biomedical materials 134 (2022) 105388

Contents lists available at ScienceDirect

Journal of the Mechanical Behavior of Biomedical Materials

journal homepage: www.elsevier.com/locate/jmbbm

# An investigation into patient-specific 3D printed titanium stents and the use of etching to overcome Selective Laser Melting design constraints

Orla M. McGee [a,b], Sam Geraghty [a,b,c], Celia Hughes [a,b], Parastoo Jamshidi [d], Damien P. Kenny [e], Moataz M. Attallah [e], Caitríona Lally [a,b,c,*]

[a] Trinity Centre for Biomedical Engineering, Trinity Biomedical Sciences Institute, Trinity College Dublin, Dublin, Ireland
[b] Department of Mechanical, Manufacturing & Biomedical Engineering, School of Engineering, Trinity College Dublin, Dublin, Ireland
[c] Advanced Materials and Bioengineering Research Centre (AMBER), Royal College of Surgeons in Ireland and Trinity College Dublin, Dublin, Ireland
[d] School of Metallurgy & Materials, University of Birmingham, Birmingham, B15 2TT, United Kingdom
[e] Children's Health Ireland at Crumlin, Dublin, Ireland

ARTICLE INFO

*Keywords:*
Cardiovascular stents
Additive manufacturing
Patient-specific
Finite element modelling
Etching

ABSTRACT

Due to limitations in available paediatric stents for treatment of aortic coarctation, adult stents are often used off-label resulting in less than optimal outcomes. The increasingly widespread use of CT and/or MR imaging for pre-surgical assessment, and the emergence of additive manufacturing processes such as 3D printing, could enable bespoke devices to be produced efficiently and cost-effectively. However, 3D printed metallic stents need to be self-supporting leading to limitations in their design.

In this study, we investigate the use of etching to overcome these design constraints and improve stent surface finish. Furthermore, using a combination of experimental bench testing and finite element (FE) methods we investigate how etching influences stent performance. Then using an inverse finite element approach the material properties of the printed and etched stents were calibrated and compared. We show that without etching the titanium stents, the inverse FE approach underestimates the stiffness of the as-built stent (E = 33.89 GPa) when compared to an average of 76.84 GPa for the etched stent designs. Finally, using patient-specific finite element models the different stents' performance were tested to assess patient outcomes and lumen gain and vessel stresses were found to be strongly influenced by the stent design and postprocessing.

Within this study, etching is confirmed as a means to create open-cell stent designs whilst still conforming to additive manufacturing 'rules' and concomitantly improving stent surface finish. Additionally, the feasibility of using an in-vivo imaging-to-product development pipeline is demonstrated that enables patient-specific stents to be produced for varying anatomies to achieve optimum device performance.

## 1. Introduction

In the past 30 years, percutaneous therapies for the treatment of congenital heart disease have evolved immensely, however, with the limited investment from industry and support from regulatory bodies there is a lack of devices specifically designed for the treatment of congenital heart disease in paediatric patients (Kenny and Hijazi, 2017). This is further evidenced by the common off-label use of commercially available adult stents in the treatment of paediatric patients, often leading to less than optimal clinical outcomes (Kenny and Hijazi, 2017; Holzer and Hijazi, 2008). A clear clinical need exists in this area of paediatrics and with the increasingly widespread use of Computed Tomography (CT) and/or Magnetic Resonance Imaging (MRI) for pre-surgical assessment and the emergence of Additive Manufacturing (AM) processes such as 3D printing, bespoke devices could be produced efficiently and cost-effectively to meet this need. This is particularly important in cases of congenital heart disease as children born with cardiovascular defects present a wide range of different anatomies and conditions that are often unique and complex (Marsden and Feinstein, 2015; Capelli et al., 2018).

AM capabilities have allowed for the design of components with reduced weight, improved mechanical performance and reduction in the cost of production (Demir and Previtali, 2017). AM techniques for medical applications, including biomedical implants, have been

* Corresponding author. Trinity Centre for Biomedical Engineering, Trinity Biomedical Sciences Institute, Trinity College Dublin, Dublin, Ireland.
*E-mail address:* lallyca@tcd.ie (C. Lally).

https://doi.org/10.1016/j.jmbbm.2022.105388
Received 16 November 2021; Received in revised form 5 July 2022; Accepted 17 July 2022
Available online 30 July 2022

expanding rapidly and 3D printing of customised patient-specific device designs are expected to revolutionise future healthcare (Lee Ventola, 2014).

In recent years, research has been carried out into the development of 3D printed polymer stents (Guerra and Ciurana, 2018; Misra et al., 2017; van Lith et al., 2016; Cabrera et al., 2017). Misra et al. developed a patient-specific polymer stent whereby 3D segmentation of medical images and in silico modelling were used to optimize the stent design (Misra et al., 2017). However, with 99% of stents used in the treatment of coronary artery disease consisting of metal balloon-expandable stents (McClean and Eigler, 2002) and the most widely deployed cardiovascular stents made of stainless steel, titanium and cobalt-chromium (Demir and Previtali, 2017; Murphy et al., 2003), there is a need for further research into the potential for AM of patient-specific metallic stents. Recently, 3D printed metallic stents have been developed in an attempt to eliminate the drawbacks of conventional stent manufacturing techniques where stents are laser cut from a tube (Demir and Previtali, 2017; Finazzi et al., 2019). These drawbacks include stent dimensions being dependent on available tubes with high production costs. Furthermore, using standard tube diameters can lead to the use of oversized stents inducing an inflammatory response when implanted (Finazzi et al., 2019; Duraiswamy et al., 2008; Zhao et al., 2009). Reduction in this inflammatory response reduces the likelihood of in-stent restenosis, the most significant long-term limitation of stenting (Kornowski et al., 1998). Metallic stents produced via AM could overcome these challenges in both production and treatment leading the way to 3D printing bespoke and unique stent designs. This would be particularly useful for paediatric patients who require unique device designs. This paired with a relatively small patient cohort and challenges related to medical device approval results in little financial incentive in the development of devices for these patients (Shibbani et al., 2016).

Selective Laser Melting (SLM) is one AM method which has already been used to 3D print metallic stents (Demir and Previtali, 2017; Finazzi et al., 2019; Wen et al., 2018). SLM is a technique whereby successive layers of powder are selectively melted using a laser beam in order to generate a specified geometry (Finazzi et al., 2019). A study by Demir & Previtali (Demir and Previtali, 2017) investigated SLM of cobalt-chromium stents for cardiovascular stenting. That study outlined rules on creating a geometry that is self-supporting and negates the need for supports in the printing of the stent. This ensures there is no unnecessary damage to the stent in removing these supports post-printing. These rules state that struts at angles greater than or equal to 45° to the horizontal, overhangs less than 1 mm, and gaps greater than 0.3 mm should be incorporated into the print designs. However, these design rules lead to restrictions in the design of stents available through AM. Furthermore, the printing of SLM stents requires further investigation as limitations to printing on the micro-scale such as resolution, surface finish and layer bonding can impact the stent performance (Ngo et al., 2018).

In this study, the use of the post processing technique, etching, and its potential to overcome these design restrictions has been investigated. Post-processing treatments applied to AM metal parts where there is removal of material can be categorized into mechanical treatments, laser-based treatments or chemical treatments (Maleki et al., 2021). In this study, chemical etching was investigated due to limitations of laser-based and mechanical treatments relating to geometric difficulties for bespoke stents.

Finite Element (FE) modelling has been used over the past two decades to investigate cardiac mechanics, hemodynamics and device design (Taylor and Figueroa, 2009). In particular, patient-specific FE models have been used to investigate cardiovascular device performance, optimal sizing, placement and optimisation of device design (Marsden and Feinstein, 2015; Capelli et al., 2018; McKenna and Vaughan, 2021; Rocatello et al., 2019; Li et al., 2013). Li et al. previously used FE methods to optimize the design of coronary stents to reduce the stent dog-boning effect (Li et al., 2013). Rocatello et al. recently demonstrated the feasibility of using a patient-specific FE model to optimize the device design of a heart valve stent frame suggesting that such methods could be used prior to the first-in-human trials to develop improved devices (Rocatello et al., 2019).

Whilst finite element modelling can be used to simulate stent implantation, the limited specific knowledge of the material properties of 'as print' stent struts at various print orientations limits their accuracy (Barba et al., 2020). This can be overcome using reverse engineering approaches to 'back out' the properties of the material based on inverse FE approaches, such as that presented in (Dennis et al., 2011).

The objective of this study was to determine the feasibility of generating patient-specific SLM stents and the use of etching to overcome design restrictions of the SLM technique. In this study, we used CT images of a 4-year old patient with a congenital heart disease known as aortic coarctation, requiring treatment with a stent. The patient's geometry was reconstructed and the design of a patient-specific stent using SLM printing techniques was investigated. Using the design rules outlined in Demir & Previtali (Demir and Previtali, 2017) two stent designs were developed and the impact of etching as a post-processing technique on the stent performance was investigated. This was done using a combination of experimental testing combined with FE modelling. Further to this, using the CT reconstructed patient geometry, a FE model was developed to simulate the deployment of the stent into the patient's anatomy and the performance of the stents pre- and post-etching were compared. To the author's knowledge, this is the first time a 3D printed open cell design has been achieved and inverse FE has been applied to investigate 3D printed metallic stent design and performance.

## 2. Materials and methods

### 2.1. Stent design

Two stents were designed in their expanded configuration based on measurements of the patient's anatomy where a lumen diameter of 10 mm was desired. The stents were designed in Solidworks (Dassault Systemes SolidWorks Corp) following rules of AM of stents based on Demir & Previtali (Demir and Previtali, 2017). The first stent design was a Simple Honeycomb (SH) stent design with a 10 mm diameter and 0.5 mm strut width and thickness shown in Fig. 1(A). The second stent design was a Novel Design (ND) using a honeycomb stent structure with a 10 mm diameter and 0.5 mm strut thickness, however, the width of the struts was varied around the circumference of the stent with all but two struts at each level of the stent having a width of 0.2 mm and two struts having a width of 0.5 mm as shown in Fig. 1(B). The two stent types were chosen to represent the extremes of stent design, that is, (i) a rigid closed cell design that conforms easily to the AM rules outlined by Demir & Previtali (Demir and Previtali, 2017) and would inherently have high radial stiffness and high bending stiffness, and (ii) an open cell design which is considerably more compliant by the nature of its design but also does not meet the AM rules in its final form.

### 2.2. Titanium powder

The powder used was Ti–6Al–4V ELI (Grade 23) (Carpenter, 2020). The powder was spherical and produced by gas atomisation. Its size distribution was 22.5–47.2 μm with an average size of 32.7 μm. The powder's chemical composition is given in Table 1:

### 2.3. Selective Laser Melting

A ReaLizer SLM 50 with a 100 W fibre laser was used to print the stent geometries in Titanium. The estimated beam diameter was in the range of 15–20 μm. The processing chamber was filled with argon gas reaching an overpressure of 15 mbar. A circulation pump was used to maintain parallel flow to the powder bed and oxygen was maintained below 12%. A modulated continuous wave laser emission was used with

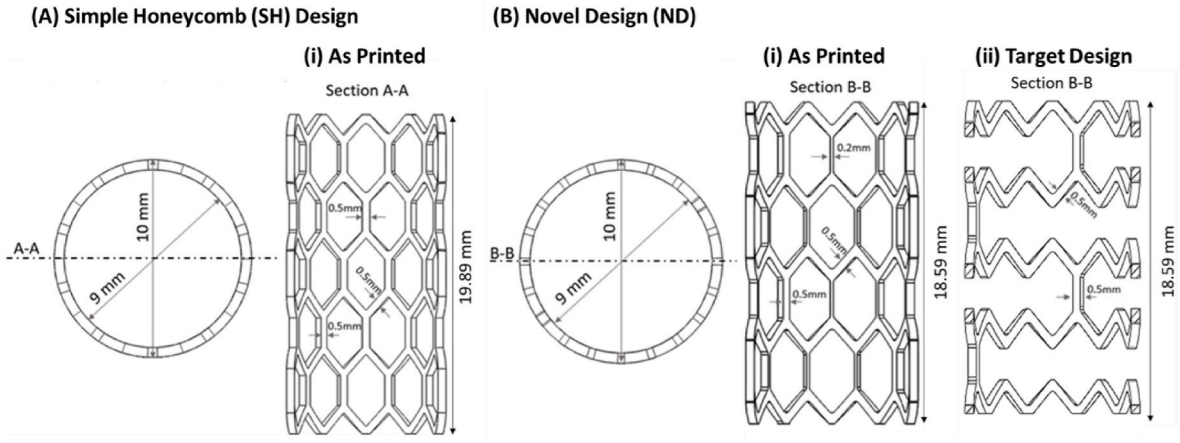


**Fig. 1.** Schematic of (A(i)) Simple Honeycomb (SH) stent design and (B) Novel Design (ND) stent design (i) with supports and (ii) without supports.

**Table 1**
Chemical composition of titanium powder.

| Element | N | C | H | Fe | O | Al | V | Ti |
|---|---|---|---|---|---|---|---|---|
| Mass Fraction (%) | 0.01 | 0.01 | 0.0027 | 0.21 | 0.11 | 6.3 | 3.9 | Bal |

an exposure time of 40 μs and a point distance of 10 μm. The laser current was maintained at 1200 mA (23.4 W) for the outer boundary and 2800 mA (67.8 W) for the inner hatching. A boundary-scan was executed first with parallel hatching scan lines with a hatch distance of 0.08 mm used internally. A layer thickness of 25 μm was kept constant throughout the build. Magics 23.02 (Materialise) was used to prepare the model. RDesigner (DMG MORI, Bielefeld, Germany) was used for setting laser trajectories and ROperator (DMG MORI, Bielefeld, Germany) was used for the machine preparation. Six of the SH stents and three of the ND stents designs were printed.

### 2.4. Post processing (etching)

Chemical etching efficiently reduces surface defects such as unmelted powder particles stuck to the built part and irregularities in layer stacking that manifest as protrusions perpendicular to the build direction (Lhuissier et al., 2016). The elimination of these defects leads to an increase in fatigue life when compared to as-built AM struts (Persenot et al., 2017). In this study, etching was used to reduce the stent strut thickness and improve the surface finish. The samples were immersed into an aqueous etching solution containing hydrofluoric and nitric acid ((HF: HNO3: H2O = 1:2:3) for 12 min and then transferred into distilled water for 5 min and rinsed with ethanol to complete the cleaning stage. Three of the SH design were etched, and all three of the ND designs were etched. The finished stent designs can be seen in Fig. 2.

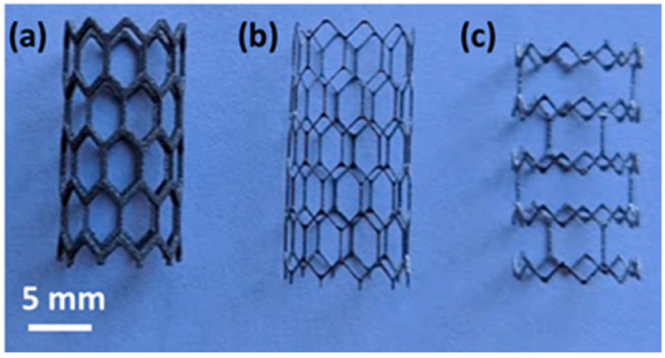


**Fig. 2.** SLM Printed stents; (a) Simple Honeycomb (SH) (b) Simple Honeycomb Etched (SHE) and (c) the Novel Design Etched (NDE).

### 2.5. Printed stent geometric dimensions

A Leica Microsystems stereoscopic microscope (accurate to 1 μm) was used to measure the width of the stents' struts (Fig. 3). For each stent, the vertical strut width, 45° strut width and strut thickness were measured with 5 measurements of each taken for an individual stent. These measurements (Table 2) were then used to create representative geometries of each individual 'as printed' and 'as etched' stents using Solidworks (Dassault Systemes SolidWorks Corp). The stents were then meshed using ANSA BETA (CAE Systems) and ABAQUS (Dassault Syst è mes Simulia Corp).

### 2.6. Experimental crush test

Using an Instron 3366, a crush resistance test using parallel plates (Fig. 4) was performed on the three groups of stents; SH, SH-etched and the ND stent designs. The stent diameter was reduced by 3 mm and the reaction force was measured to quantify the stiffness of the different stents. A preload of 1.06 N was applied to each stent (0.56 N load as a result of the Perspex plate weighing 57.73 g and 0.5 N preload applied by the machine).

### 2.7. Stent surface roughness

Scanning Electron Microscopy (SEM) images of the stents were taken after the crush test was performed to investigate the surface roughness of the stents. Additionally, White Light Interferometry (WLI) was used to assess the relative surface roughness of each of the stents to investigate differences between printed and etched stents and the variation of roughness between the strut directions within the stent designs. A Filmetrics ProFilm 3D optical profilometer was used and arithmetical average roughness for a given path, $R_a$, was used to compare surface quality.

ISO 4288:1996 recommends a roughness sampling length of 0.8 mm and a roughness evaluation length of 4 mm for $R_a$ values greater than 0.1 μm and less than or equal to 2 μm, corresponding to the $R_a$ range for the etched stents. Similarly, the ISO standard (ISO - ISO 4288, 1996) specifies a roughness sampling length of 2.5 mm and roughness evaluation length of 12.5 mm for $R_a$ values greater than 2 μm and less than or equal to 10 μm, corresponding to the $R_a$ range for the unetched stents. Due to limitations related to the length of the diagonal struts, it was not possible to attain this recommended sampling length. To mitigate this a consistent sample length of 600 μm was used across all measured struts and in a similar fashion to (Van Hooreweder et al., 2017) and the effect

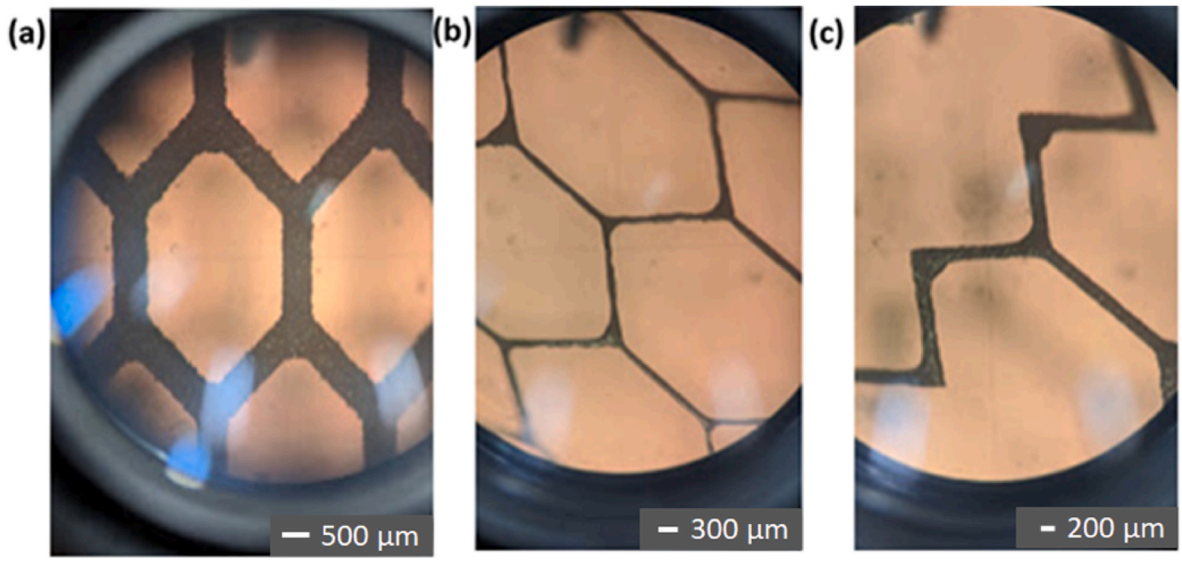


**Fig. 3.** Stereoscopic images of stents' struts of (a) Simple Honeycomb (SH) (b) Simple Honeycomb Etched (SHE) and (c) the Novel Design Etched (NDE) stent designs.

**Table 2**
Stereoscopic measurements of stent vertical width (W1), width at the 45° (W2) and thickness.

| Stent Design | | W1 (μm) | | W2 (μm) | | Thickness (μm) | |
|---|---|---|---|---|---|---|---|
| | | Average | Std Dev | Average | Std Dev | Average | Std Dev |
| **SH** | **SH1** | 529 | 40 | 558 | 48 | 573 | 19 |
| | **SH2** | 544 | 23 | 560 | 25 | 590 | 16 |
| | **SH3** | 537 | 20 | 563 | 23 | 576 | 39 |
| | **Average** | 537 | 27 | 560 | 32 | 580 | 26 |
| **SHE** | **SHE1** | 95 | 8 | 102 | 33 | 138 | 37 |
| | **SHE2** | 156 | 28 | 133 | 30 | 169 | 24 |
| | **SHE3** | 152 | 15 | 124 | 33 | 149 | 64 |
| | **Average** | 135 | 34 | 120 | 32 | 152 | 43 |
| **NDE** | **NDE1** | 239 | 22 | 238 | 17 | 234 | 9 |
| | **NDE2** | 176 | 16 | 225 | 16 | 231 | 25 |
| | **NDE3** | 169 | 27 | 239 | 28 | 273 | 50 |
| | **Average** | 195 | 39 | 234 | 20 | 246 | 36 |

of the low-test length was neglected as the measurements were used comparatively.

Eight struts, four vertical struts and four diagonal struts from each sample were scanned at a length of 600 μm. These images were obtained at 50× magnification, giving a field of view of 0.4× 0.34 mm. Two scans were taken with a back-scan length of 110 μm and then stitched together with the provided profilometer software to achieve the prescribed sample length. The stitched images provided a 3D map of the surface topography which was then processed within the software package to remove outliers whereby pixels with a slope above 60° were removed and invalid pixels were filled in. The line roughness tool was then used to calculate a $R_a$ value along the strut within the scan length. Additional microscopy images at 10× and 50× magnification were taken for further qualitative comparison of surface roughness and defects.

### 2.8. Finite element crush test

A FE model was created to replicate the experimental crush test using ABAQUS Standard 2017 (Dassault Systemes SolidWorks Corp). Two parallel plates 45 × 45 mm were meshed using (SFM3D4) 4-noded quadrilateral surface elements. The stent was placed between the two plates as seen in Fig. 9(a). Zero friction and hard normal contact were assigned between the stent and the plates. The bottom plate was fixed, and the top plate was displaced −3 mm in the y-direction to replicate the displacement in the crush test. The material properties used were linear elastic with a Young's modulus that was determined using the inverse FE approach outlined in Section 2.9 and a Poisson's ratio of 0.31 (Carpenter, 2020; Falkowska et al., 2020). This test was used to test the SH design, SH-etched design, and the ND stents. A mesh dependency was performed on each variation of the stent design whereby a 100% increase in mesh density led to <2% change in the final reaction force.

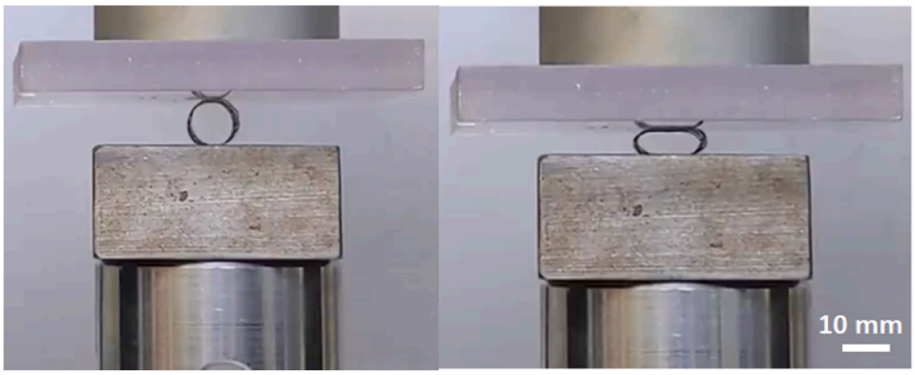


**Fig. 4.** Experimental parallel plate crush test.

### 2.9. Inverse finite element analysis

Calibration of the Young's modulus for each of the stents was carried out using an optimisation loop in MATLAB (MathWorks, MA, USA). An initial estimate of the Young's modulus for each stent was made based on the experimental crush tests. This value was then used in the crush test simulation and the force-displacement results were then compared to the experimental data in the linear elastic region by calculating the Root Mean Square Error (RMSE). This process was repeated until the solver reached the lower bound tolerance of $1e^{-4}$ for the RMSE value.

### 2.10. Patient-specific finite element model of stent deployment

Fully anonymised CT scan data of the aortic arch of a paediatric patient with an aortic coarctation, necessitating the placement of a stent, were obtained from our clinical collaborator. Image segmentation was applied to this CT data to extract a computer-aided design (CAD) representation of the patient geometry using 3D Slicer (Fedorov et al., 2012). A skin surface of the vessel was then constructed with ANSYS SpaceClaim (ANSYS Inc) and finally, a volumetric hexahedral mesh representation of the geometry was generated with ANSA BETA Pre-Processor (CAE Systems) (Fig. 5). The aortic arch was assigned a uniform thickness of 1 mm (Creane et al., 2011) and was meshed using (C3D8R) 8-node linear brick elements with reduced integration and hourglass control. A mesh dependency analysis was performed on the aortic arch and it was found there was a 1.9% change in the max von Mises stress and a 2.4% change in the average von Mises stress with a 59% increase in the mesh density.

Using ABAQUS Explicit a finite element model was used to simulate the deployment of the three stents into the patient's anatomy. The stents were modelled as linear elastic titanium and meshed as in the FE crush test. The patient's aortic arch was modelled using an incompressible hyperelastic isotropic Mooney–Rivlin model. The model was defined using the following strain energy density function, U:

$$U = C_{10}(\overline{I}_1 - 3) + C_{01}(\overline{I}_2 - 3) + \frac{1}{D}(J-1)^2$$

where $C_{10}$ and $C_{01}$ are material parameters, D is the incompressibility parameter and $I_1$ and $I_2$ are the first and second invariant of the right Cauchy–Green deformation tensor, $\boldsymbol{C}$:

$$\overline{I}_1 = tr(\boldsymbol{C})\ \overline{I}_2 = \frac{1}{2}\left[\overline{I_1}^2 - tr(\boldsymbol{C}^2)\right]$$

D was assigned a value of $1e^{-6}$ assuming near incompressibility (Jermihov et al., 2011; Gunning et al., 2014). The material constants $C_{10}$ = 0.5516 MPa and $C_{01}$ = 0.1379 MPa were adopted from (Auricchio et al., 2014; Einstein et al., 2003; Gunning et al., 2014).

Using a cylindrical part (crimper) meshed using (SFM3D4R) 4-noded quadrilateral surface elements with reduced integration and a local cylindrical coordinate system created to displace the crimper radially inward. Hard normal contact with a coefficient of friction of 0.8 was applied between the stent and the crimper (Qiu et al., 2018). The crimper was assigned as the master surface, and the frame was assigned as the slave surface.

The top and bottom edges of the aortic arch were constrained using displacement boundary conditions in the longitudinal and circumferential directions. The stent was uncrimped and hard normal, frictionless contact was applied between the stent and the aorta (Lally et al., 2005). The kinetic energy of the simulations was monitored to ensure that the ratio of kinetic energy to internal energy remained less than 5%. This criterion was proposed by (Choi et al., 2002) and ensures that the dynamic effects are negligible.

The patient-specific model was used to compare the performance of all three stent designs and examine the material properties that were calibrated using the inverse FE approach. It must be noted that as this was a feasibility study none of these stents were implanted in the patient.

### 2.11. Statistical analysis

Statistical analysis was performed using GraphPad Prism 9 statistical software (GraphPad Software Inc) with the aim of investigating and quantifying statistically significant differences between as built and etched stents and, between vertical and diagonal struts. To investigate statistically significant differences between the means of each group a Welch's *t*-test with a 95% confidence interval was applied. This test method assumes the means of the compared populations are normally distributed and is insensitive to equality of variance. The t-tests estimate with 95% confidence that there is a statistically significant difference between each of the stent groups.

## 3. Results

### 3.1. As printed and As etched stent geometries

#### 3.1.1. Geometric differences

Stereoscopic measurements of the as printed SH stent geometries found that stents had increased width and thickness compared to the STL input. It was found that the thickness of the stents showed the greatest increase, averaging 80 ± 26 μm. In struts printed at 45°, an average

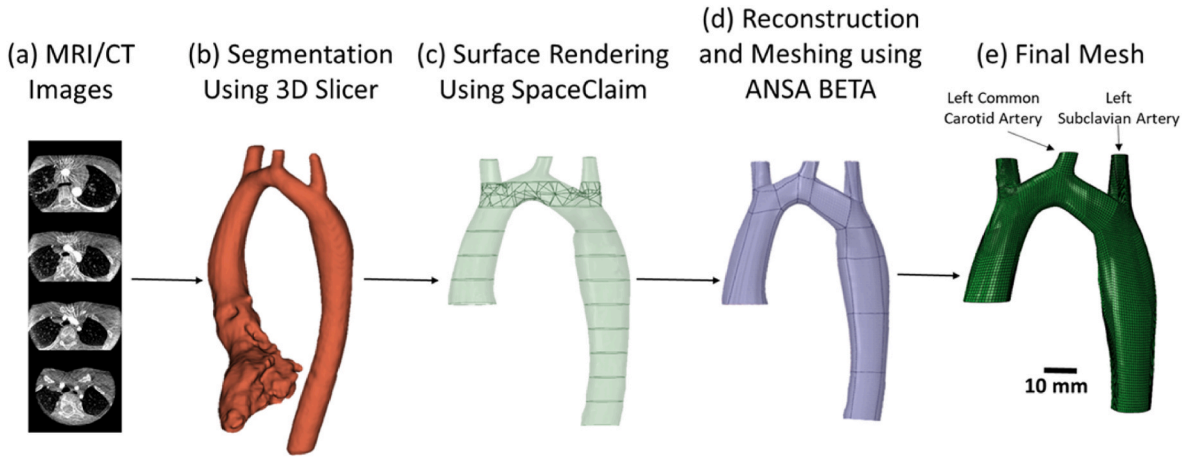


**Fig. 5.** Steps used to generate a patient-specific finite element mesh for CT data of a patient. (a) CT/MRI images (b) segmentation using 3D Slicer (c) surface rendering using SpaceClaim (d) reconstruction and meshing using ANSA BETA (e) final meshed geometry.

increase of 60 ± 32 μm in width was observed compared to an average increase of 37 ± 27 μm in width in struts printed vertically.

Etching was found to successfully remove material from the width and thickness of the stents leading to an average thickness of 152 ± 43 μm for the SHE and 246 ± 36 μm for the NDE stents. The average width of struts at 45° was found to be 120 ± 32 μm for the SHE and 234 ± 20 μm for the NDE while the vertical strut widths were found to be 135 ± 34 μm and 195 ± 39 μm for the SHE and NDE, respectively. Furthermore, the 200 μm struts present in the NDE stent prior to etching were completely removed as a result of etching. This led to an open-cell stent design that to the author's knowledge has not previously been achieved through 3D printing.

#### 3.1.2. Surface roughness

In addition to the removal of material from the thickness and width of the stent, etching led to an improvement in surface roughness. Fig. 6 demonstrates an SEM image of a stent pre- and post-etching where the improvement in the surface finish after etching is evident. Un-melted powder particles and irregularities in layer stacking were successfully removed using chemical etching upon visual inspection.

WLI was performed to quantify the improvement in surface roughness evident from SEM images and investigate the relationship between print angle and surface roughness. A box and whisker plot of the arithmetical average roughness, $R_a$, for each stent group is presented in Fig. 7(a). In terms of mean and standard deviation the $R_a$ values for the SH, NDE and SHE were measured as 3.76 ± 0.27 μm, 1.13 ± 0.14 μm and 0.39 ± 0.06 μm, respectively. It was found that using a Welch's *t*-test as described in section 2.11 that there is a statistically significant difference between each of the stent groups.

Fig. 7(b) presents a box and whisker plot of the $R_a$ value of each stent group separated by the two strut directions, namely the vertical (V) and diagonal (D) directions. It was found that using a Welch's *t*-test as described in section 2.11 that there is no statistical difference between each of the horizontal and diagonal struts.

### 3.2. Experimental crush test

The results of the experimental crush test are shown in Fig. 8. The results demonstrate the influence that etching has on stent performance. It must be noted that a fractured strut in the 45° strut was observed in SHE-1 prior to the experimental crush test, the 45° struts are linked with the radial stent stiffness and would be expected to lead to a reduction in stent stiffness. It must also be noted that due to a lack of symmetry in the NDE stents greater variation is seen in the crush test results when compared to the SH and SHE stent designs.

### 3.3. Finite element crush test and material calibration

Fig. 9 (b), (c) and (d) show the force displacement curves of the experimental crush test to the corresponding FE prediction using the calibrated Young's modulus for the different stent designs. Table 3 presents the Young's modulus and corresponding RMSE values calculated using the inverse FE approach outline in Section 2.9. The SH designs show a decreased stiffness compared to the SHE and NDE stents. The average Young's modulus (E) for the SH stent was found to be 33.89 GPa when compared to an average of 76.84 GPa for the SHE stent designs. The SHE-1 design was not included due to the fact that the broken strut could not be accurately represented in an FE model and would have inaccurately influenced the material characterisation.

### 3.4. Patient-specific finite element model of stent deployment

The patient-specific model was used to compare the performance of the three stent designs and examine the material properties that were calibrated using the inverse FE approach. Six designs were investigated and the average Young's moduli from the SHE (76.84 GPa) and SH (33.89 GPa) stent designs were examined using the model. The models investigated the SH-as printed (E = 33.89 GPa), SH-as printed (E = 76.84 GPa), SH-STL (E = 33.89 GPa), SH-STL (E = 76.84 GPa), SHE (E = 76.84 GPa) and NDE (E = 76.84 GPa) stent designs. Stent performance was investigated in terms of stress in the aorta and lumen gain. Fig. 10 displays contour plots of von Mises stress in the aortic arch for each different stent design. It can be seen that the NDE and SHE stents result in lower stress distributions in the aortic arch than the SH stent designs.

The section of the aortic arch between the left subclavian artery and the left common carotid artery was examined to investigate lumen gain and maximum von Mises stress (Table 4). It was found that while the SHE design reduced stress it also led to a lower increase in lumen area. Further to this, it was found SH 'as print' design led to the greatest increase in maximum von Mises stress and the greatest increase in lumen area.

Finally, a percentage volume plot demonstrating the percentage

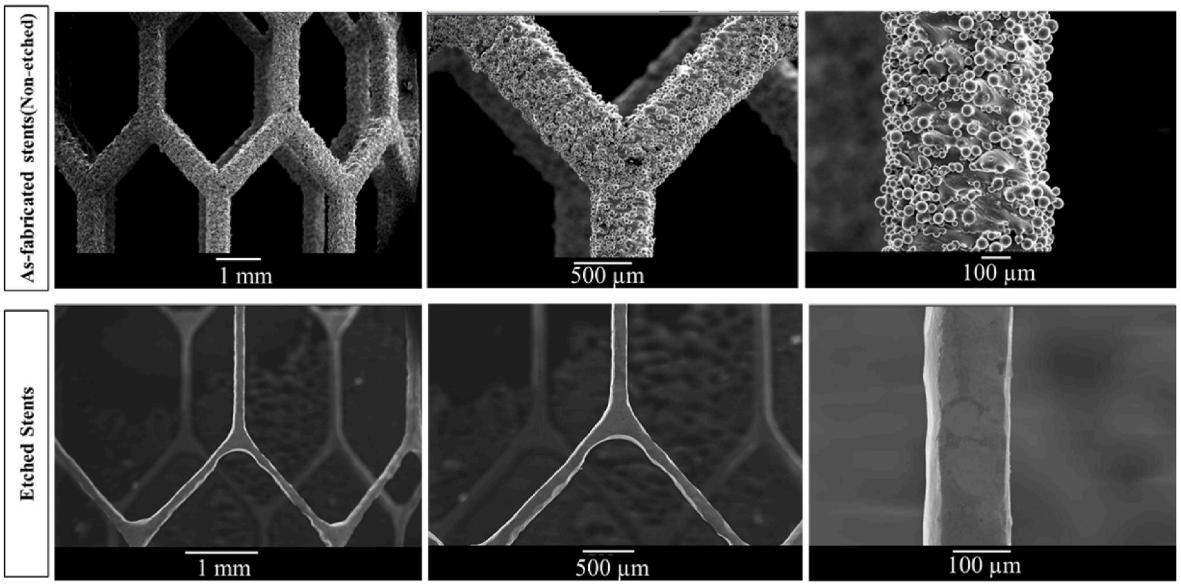


**Fig. 6.** SEM micrographs of Honeycomb stents, showing the effects of chemical etching on surface cleaning and reduction of strut size. In as-fabricated status (top row) and after etching (bottom row).

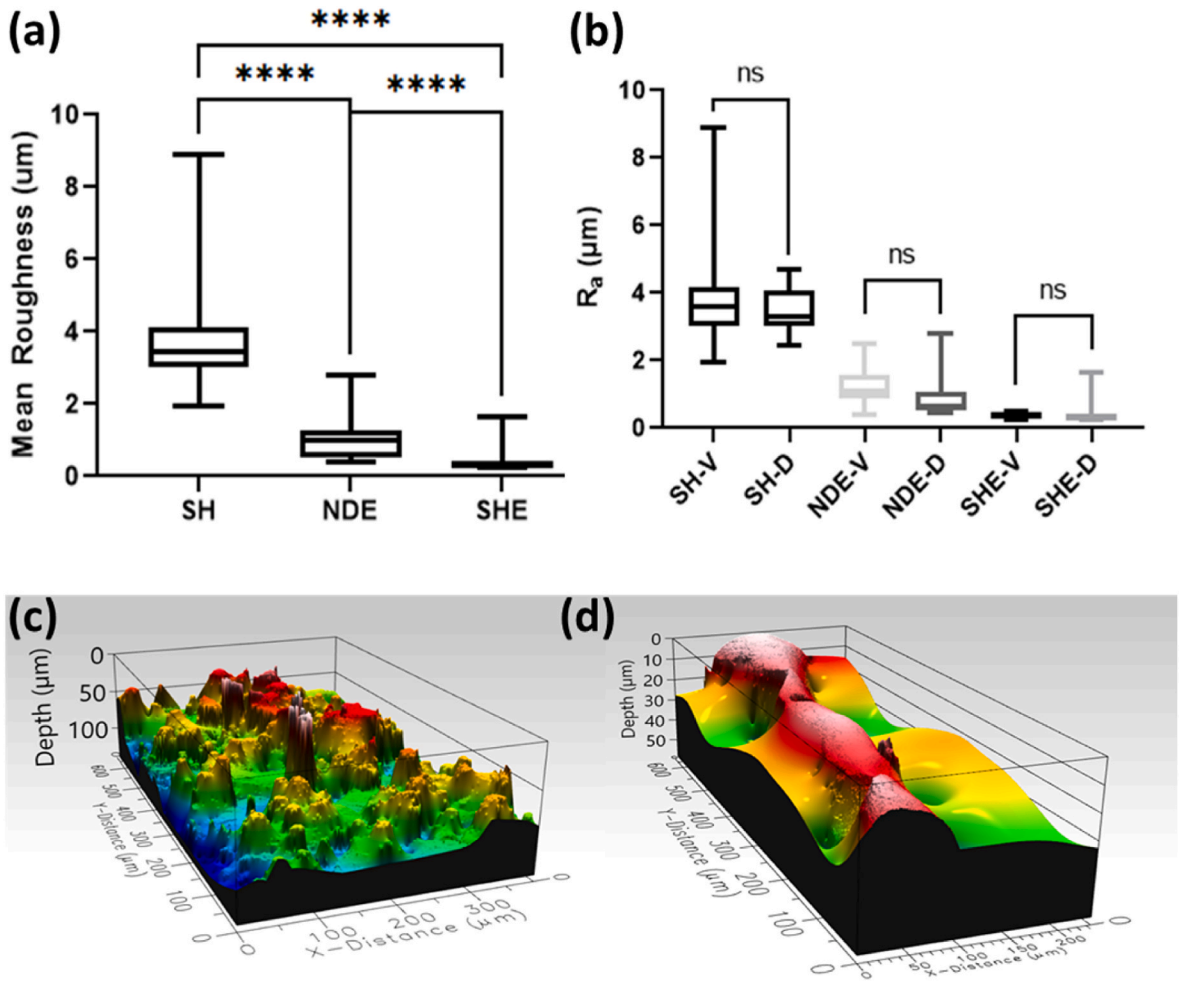


**Fig. 7.** (a) Box and whisker plot of arithmetical average surface roughness, $R_a$ (µm) and results of Welch's *t*-test for Simple Honeycomb (SH), Simple Honeycomb Etched (SHE) and the Novel Design Etched (NDE). **** indicates a p-value less than or equal to 0.0001. (b) Box and whisker plot of arithmetical average surface roughness $R_a$ (µm) and results of Welch's *t*-test for vertical (V) and diagonal (D) strut directions for each stent group. ns indicates no statistically significant difference between means. (c) WLI 3D surface map of an SH stent strut and (d) SHE stent strut.

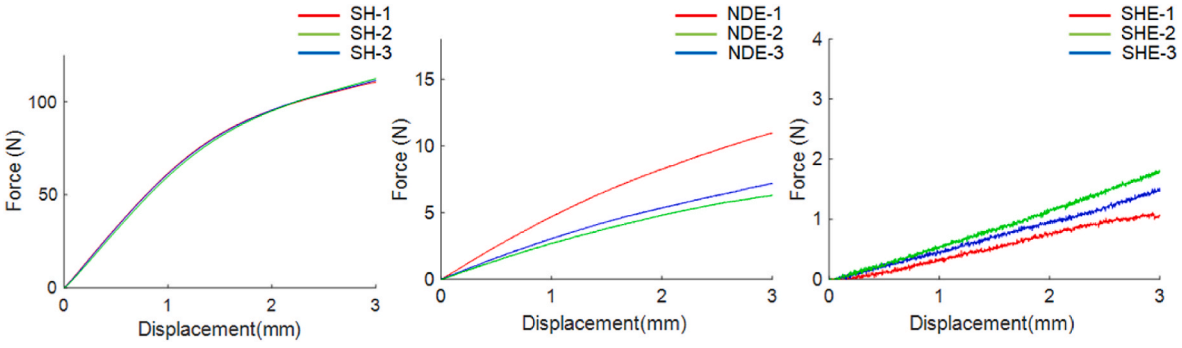


**Fig. 8.** Force-displacement curve from the experimental crush test of the printed stents.

volume of tissue at different bands of von Mises stress was used to examine the stress distribution in the tissue between the left subclavian artery and the left common carotid artery (Fig. 11). It was found the SHE and NDE designs led to a considerable reduction in the stresses observed in the tissue.

## 4. Discussion

In this study, we have investigated the use of SLM printing to design patient-specific stents. Using FE methods, the performance of these stents was assessed alongside experimental bench tests. FE methods were further used to compare the performance of the stents post-deployment in the patient's anatomy. Although there is still much to be investigated for the full potential of SLM printed stents to be realised, this study demonstrates the suitability of the methods outlined for use in the design of SLM printed stents for patient-specific purposes, in particular, in relation to paediatric patients. The results of this study demonstrate the ability of post-processing techniques such as etching to

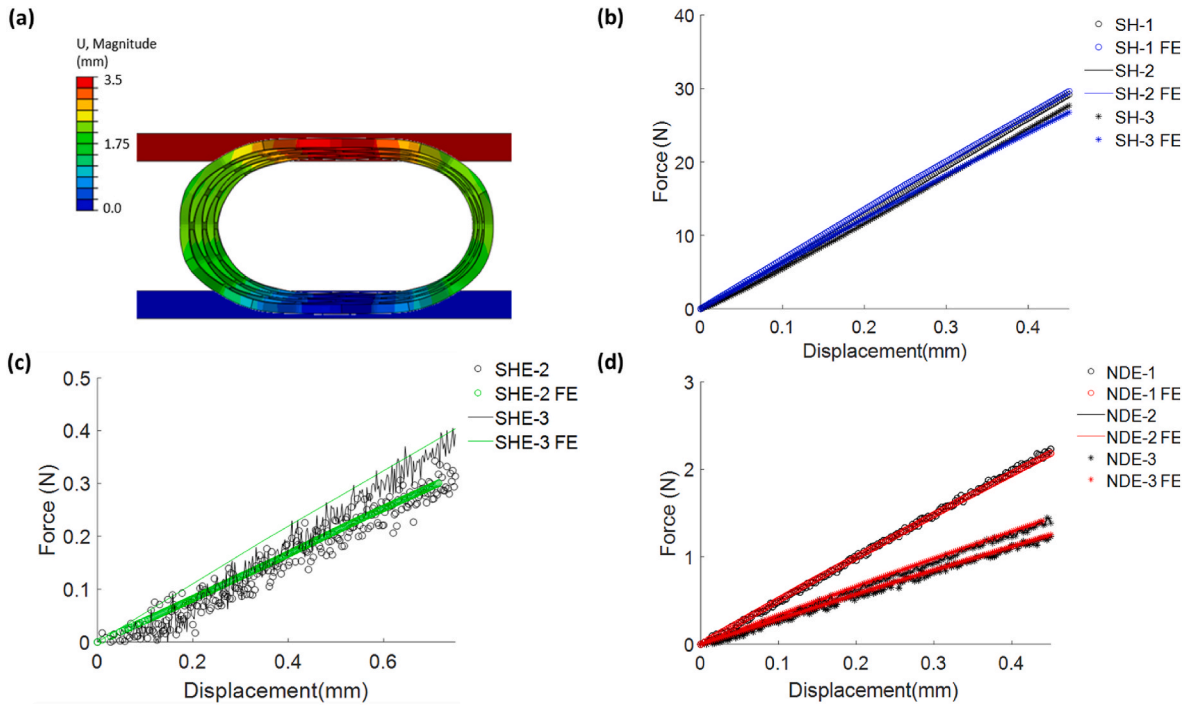


**Fig. 9.** (a) Contour plot of displacement for the finite element model of the crush test of SH stent. Force-displacement curve from the experimental crush test results and finite element (FE) predictions for (b) SH (c) SHE and (d) NDE stent designs.

**Table 3**
Calibrated Young's Modulus and corresponding RMSE value for each stent design.

| Stent Design | Youngs Modulus (GPa) | RMSE |
|---|---|---|
| SH1 | 35.8 | 0.447 |
| SH2 | 33.8 | 0.576 |
| SH3 | 31.1 | 0.703 |
| SHE2 | 55.0 | 0.024 |
| SHE3 | 98.7 | 0.284 |
| NDE1 | 110.5 | 0.042 |
| NDE2 | 114.0 | 0.020 |
| NDE3 | 64.0 | 0.023 |

overcome design limitations that are inherent to the SLM technique and to better control the stent designs available through AM.

Several limitations and assumptions have been made throughout this study, firstly it must be noted that this study was used to examine only the processes and techniques outlined in the paper. Further investigation and studies must be carried out before the stents developed will be suitable for implantation in a patient. The implantation in this paper was only examined virtually and these stents were not tested *in vivo*. It must also be noted that the properties for titanium used in this model are linear elastic material properties however, the stents would likely undergo plastic deformation during stent deployment. It must be noted that the material calibration was used to highlight how overestimation of stent dimensions due to melted powder particles and irregularities in layer stacking can lead to different outcomes and this was adequately achieved despite the use of a linear elastic approach. Similarly, the aortic arch was modelled as a hyperelastic isotropic material although it is known that arterial tissue exhibits anisotropic behaviour (Vossoughi et al., 1982). However, the constitutive laws used were fitted to the circumferential direction, the stiffest directions of the aortic root, and it is known that the aortic root responds to stent deployment predominantly in the circumferential direction. Therefore, the use of an isotropic model was considered to be appropriate for correctly capturing the stress in this model (Gunning et al., 2014; McGee et al. 2018; Zahedmanesh et al., 2010). Moreover, this model was only used for comparison purposes of the stent designs. It must also be noted the stents modelled were taken as approximate measurements of the thickness and width of the stents and the variations in measurement observed throughout the stent were not modelled. However, this approximation was deemed valid as several measurements were taken from different struts throughout each stent geometry and microscopic measurements were deemed preferable to CT due to concerns over beam hardening and blooming effects when taking CT of titanium (Kasparek et al., 2019). Finally, it must be noted that the Ti-64 was used predominantly for 'proof-of-concept' purposes and future work will include the investigation of other metal powders, such as Nitinol, to optimize cardiovascular stent designs.

One of the main findings of this study was a novel method to overcome some of the constraints in SLM printing where stents need to be self-supporting. Using thinner struts that can be etched away can generate a different design and create new capabilities for 3D printed stents, even allowing the creation of open-cell designs. Open-cell designs can be advantageous in reducing obstruction to branching arteries and can better conform to tortuous arteries as they have superior flexibility to closed cell designs (Lally et al., 2006). It must be noted that although only a crush test was carried out to assess stent performance in this study, future work will include a more exhaustive analysis of stent performance and include 3-point bend testing to more quantitively assess the stent bending stiffness.

Further to this, using etching, thinner strut widths and thicknesses can be achieved which can lead to a reduction in stiffness of the overall stent performance, as shown in the experimental crush tests. The strut thickness that can be achieved with SLM printing is dependent on several limiting factors including laser spot size and resolution (Demir and Previtali, 2017; Finazzi et al., 2019). This can be seen in the results where we see +80 μm when printing 500 μm struts. However, commercial stent struts range from 80 to 140 μm (Jiménez and Davies, 2009). Using etching can further reduce the thickness of struts to levels that cannot be successfully achieved during printing. The average reduction in thickness after etching can be calculated from Table 2 and was found to be 57.6% for NDE and 73.8% for SHE stents.

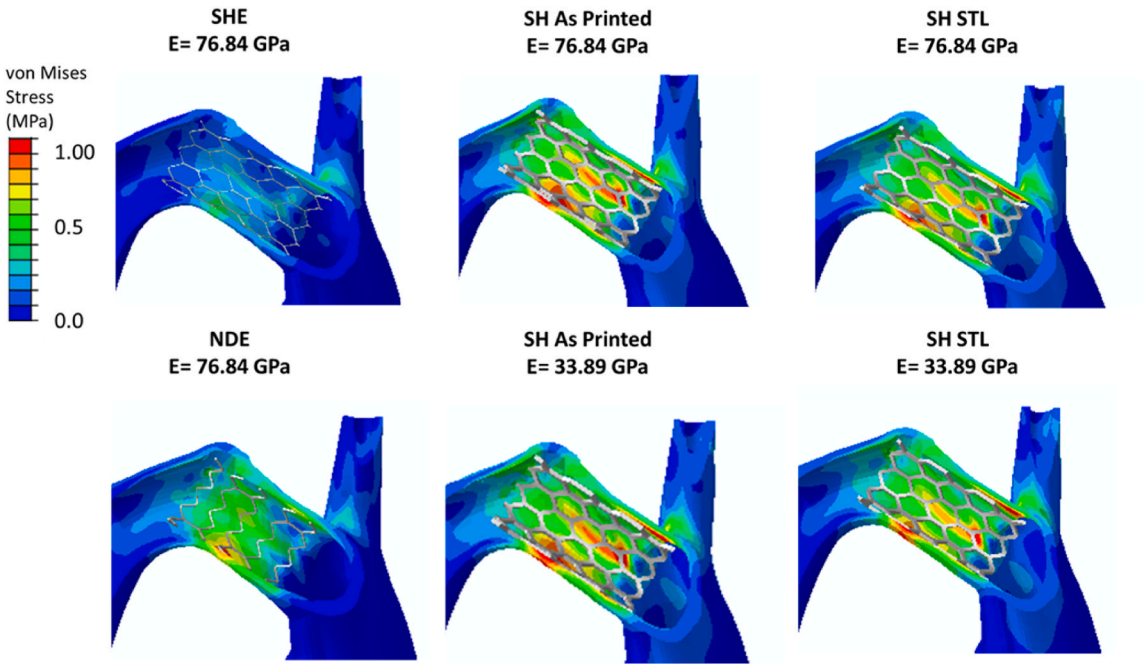


**Fig. 10.** Contour plots of von Mises stress in the aorta post-deployment of different stent designs.

**Table 4**
Maximum von Mises stress and Increase in Lumen Area for the different stent designs and stiffnesses.

| Stent | Increase in Lumen Area ($mm^2$) | Maximum Von Mises Stress (MPa) |
|---|---|---|
| SH STL (E = 33.89 GPa) | 2.97 | 1.096 |
| SH STL (E = 76.84 GPa) | 3.03 | 1.102 |
| SH as print (E = 33.89 GPa) | 3.11 | 1.168 |
| SH as print (E = 76.84 GPa) | 3.14 | 1.169 |
| SHE (E = 76.84 GPa) | 1.08 | 0.444 |
| NDE (E = 76.84 GPa) | 1.61 | 0.83 |

Furthermore, etching was found to significantly improve stent surface roughness which can improve fatigue life (Persenot et al., 2017). A reduction in surface roughness of 3.37 μm was achieved between the SH and the SHE stents, where SHE stents had a surface roughness of 0.39 ± 0.06 μm. This is a distinct improvement on previously published $R_a$ values of 2.2 μm measured post electropolishing in a recent study (Finazzi et al., 2020). Surface roughness values for SHE and NDE stent designs were also statistically significantly different from one another. It must be noted that the SHE stents and NDE stents were etched using the same procedure. However, the two stent designs were etched on different days using different batches of etchant. This raises questions regarding the repeatability of the current etching procedure and future work will include a more robust etching study examining the repeatability and reproducibility of the etching protocol. Furthermore, etching led to variation in the width and thickness throughout individual struts. This is currently a major limitation to the 3D printing and etching process as stent width and thickness need to be controlled. Future work will also include examining methods to improve the consistency of material removal throughout a stent. In addition to examining surface finish to improve stent fatigue life, fatigue life can also be improved through heat treatment (Sing et al., 2020; Fragoudakis et al., 2014; Niinomi and Akahori, 2010; Vrancken et al., 2012). Heat treatment was outside of the scope of this study, but future work will examine heat treatment and its influence on the mechanical properties and fatigue life of the 3D printed stents.

The experimental crush test demonstrates a clear reduction in the overall radial stiffness of the stent post-etching. However, the material calibration of the reconstructed 'as printed' and 'as etched' stent designs found the material in the SH (non-etched) stents to be more compliant. In fact, both the SHE and SH stents were printed at the same time under the same conditions and print parameters. The reason for this perceived increase in compliance can be attributed to melted powder particles and irregularities in layer stacking contributing to increased stent dimensions but not contributing to the stent's load-bearing ability and the overall stent performance. It must also be noted when examining the RMSE values for the SH stent, that the values achieved were higher than those observed for the SHE and NDE stents. This further supports the argument that the dimensions taken from these stents do not accurately represent the amount of load-bearing material. Such discrepancies in the amount of load-bearing material must be carefully considered when predicting SLM stent performance.

Finally, the stent performance was tested in a patient-specific FE model. This was used to assess the difference in the performance of the different stent designs and different material properties of the stents. Table 4 demonstrates the increase in lumen area and maximum von Mises stress for each of the stents designs and material combinations. Additionally Figs. 10 and 11 demonstrate the stress distribution through the aortic root. Fig. 11 quantitively shows the percentage volume of tissue under different bands of stress for the different stents and it can be seen that for the etched stents a smaller volume of tissue is under higher levels of stress. Higher stress levels can be linked to issues such as in-stent restenosis (Chen et al., 2009). It was found that the 'as printed' SH stent gave the greatest lumen area gain which can be attributed to the stents' thicker struts when compared to the etched stents and the fact that etching itself reduced the diameter of the stents. However, it also led to the highest stresses in the aorta. In contrast, the SHE stents design led to the lowest gain in lumen area with the lowest stress experienced in the aorta. The advantage of the NDE design can be seen in the reduction of the occlusion to the branching left common carotid artery in Fig. 10.

It is important to note, that the SH and NDE designs are not optimal, as they are relatively stiff, particularly in bending. These stents were chosen as they conform to the AM rules outlined in Demir et al. (Demir

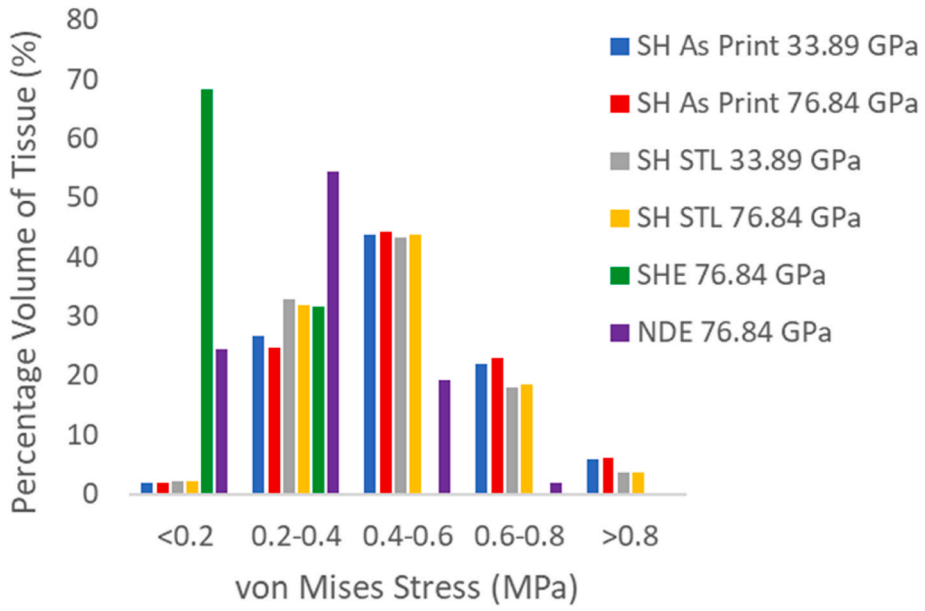


**Fig. 11.** Percentage of volume graph for the different stent designs and stiffnesses showing the stress distribution between the left subclavian artery and the left common carotid artery.

and Previtali, 2017) and the objective of this study was to demonstrate that maintaining those rules does not severely limit design when the stent is designed to incorporate etching to remove struts. However, the NDE design leads to the corner between two 45° struts widening along the thickness and creates the presence of a sharp angle. The findings of this study combined with topology optimisation through FE will allow for the creation of more optimized flexible stent designs tailored to improve patient outcomes.

## 5. Conclusion

SLM printing of stents is an area of growing research which has the potential to lead to substantial improvements of patient outcomes in its ability to rapidly develop bespoke stents. However, many limitations exist regarding restriction in printed designs, control of strut width and thickness and the fatigue life of SLM stents. This study has investigated methods to overcome these design restrictions and improve surface finish linked to stent fatigue life. However, SLM stents suitable for patient implantation will not be realised until greater control over the finished stent product is achieved. This requires further research to achieve greater control over as printed designs and post-processing techniques. Using FE methods to greater understand SLM printed stent performance, predict stent behaviour, and inform SLM printed stent design has the potential to expedite the advances needed in designing bespoke SLM stents.

## CRediT authorship contribution statement

**Orla M. McGee:** Writing – review & editing, Writing – original draft, Supervision, Software, Methodology, Investigation, Formal analysis. **Sam Geraghty:** Writing – review & editing, Writing – original draft, Visualization, Methodology, Formal analysis. **Celia Hughes:** Software, Methodology, Investigation. **Parastoo Jamshidi:** Writing – review & editing, Methodology, Investigation. **Damien P. Kenny:** Writing – review & editing, Methodology, Investigation, Funding acquisition, Conceptualization. **Moataz M. Attallah:** Writing – review & editing, Supervision, Investigation, Funding acquisition, Conceptualization. **Caitríona Lally:** Writing – review & editing, Supervision, Resources, Project administration, Investigation, Funding acquisition, Conceptualization.

## Declaration of competing interest

The authors declare that they have no known competing financial interests or personal relationships that could have appeared to influence the work reported in this paper.

## Data availability

Data will be made available on request.

## Acknowledgements

This study was funded National Children's Research Centre, Crumlin (Grant No. G/19/3), an Irish Research Council Government of Ireland Postdoctoral Fellowship (2019) (GOIPD/2019/222) and from research supported in part by a research grant from Science Foundation Ireland (SFI) under the grant number 12/RC/2278_2. Prof. Moataz M. Attallah and Dr Parastoo Jamshidi acknowledge the support from Engineering and Physical Science Research Council (EPSRC) (Grant Number: EP/R001650/1; Title: Smart peripheral stents for the lower extremity–design, manufacturing and evaluation).

## References

ANSYS Inc., "SpaceClaim." Canonsburg, Pennsylvania, United States.

Auricchio, F., Conti, M., Ferrara, A., Morganti, S., Reali, A., Feb. 2014. Patient-specific simulation of a stentless aortic valve implant: the impact of fibres on leaflet performance. Comput. Methods Biomech. Biomed. Eng. 17 (3), 277–285. https://doi.org/10.1080/10255842.2012.681645.

Barba, D., Alabort, C., Tang, Y.T., Viscasillas, M.J., Reed, R.C., Alabort, E., Jan. 2020. On the size and orientation effect in additive manufactured Ti-6Al-4V. Mater. Des. 186, 108235 https://doi.org/10.1016/j.matdes.2019.108235.

Cabrera, M.S., Sanders, B., Goor, O.J.G.M., Driessen-Mol, A., Oomens, C.W.J., Baaijens, F.P.T., Mar. 2017. Computationally designed 3D printed self-expandable polymer stents with biodegradation capacity for minimally invasive heart valve implantation: a proof-of-concept study. 3D Print. Addit. Manuf. 4 (1), 19–29. https://doi.org/10.1089/3dp.2016.0052.

BETA Cae Systems, "ANSA." Luzern, Switzerland.

Capelli, C., et al., Feb. 2018. Patient-specific simulations for planning treatment in congenital heart disease. Interface Focus 8 (1). https://doi.org/10.1098/rsfs.2017.0021.

Carpenter, Additive, 2020. PowderRange Ti64 Datasheet [Online]. Available: https://www.carpenteradditive.com/powderrange-powders.

Chen, H.Y., Hermiller, J., Sinha, A.K., Sturek, M., Zhu, L., Kassab, G.S., 2009. Effects of stent sizing on endothelial and vessel wall stress: potential mechanisms for in-stent

restenosis. J. Appl. Physiol. 106 (5), 1686–1691. https://doi.org/10.1152/japplphysiol.91519.2008.
Choi, H.H., Hwang, S.M., Kang, Y.H., Kim, J., Kang, B.S., 2002. Comparison of implicit and explicit finite-element methods for the hydroforming process of an automobile lower arm. Int. J. Adv. Manuf. Technol. 20 (6), 407–413. https://doi.org/10.1007/s001700200170.
Creane, A., Maher, E., Sultan, S., Hynes, N., Kelly, D.J., Lally, C., Dec. 2011. Prediction of fibre architecture and adaptation in diseased carotid bifurcations. Biomech. Model. Mechanobiol. 10 (6), 831–843. https://doi.org/10.1007/s10237-010-0277-8.
Dassault Systèmes Simulia Corp., "ABAQUS." (Providence, Rhode Island).
Dassault Systemes SolidWorks Corp., "SolidWorks." Waltham, Massachusetts, USA.
Demir, A.G., Previtali, B., 2017. Additive manufacturing of cardiovascular CoCr stents by selective laser melting. Mater. Des. https://doi.org/10.1016/j.matdes.2017.01.091.
Dennis, B.H., Jin, W., Dulikravich, G.S., Jaric, J., 2011. Application of the finite element method to inverse problems in solid mechanics. Int. J. Struct. Chang. SOLIDS – Mech. Appl. 3 (2), 11–21.
Duraiswamy, N., Cesar, J.M., Schoephoerster, R.T., Moore, J.E., Jan. 2008. Effects of stent geometry on local flow dynamics and resulting platelet deposition in an in vitro model. Biorheology 45 (5), 547–561. https://doi.org/10.3233/BIR-2008-0497.
Einstein, D.R., Reinhall, P., Nicosia, M., Cochran, R.P., Kunzelman, K., 2003. Dynamic finite element implementation of nonlinear, anisotropic hyperelastic biological membranes. Comput. Methods Biomech. Biomed. Eng. 6 (1), 33–44. https://doi.org/10.1080/1025584021000048983.
Falkowska, A., Seweryn, A., Skrodzki, M., Nov. 2020. Strength properties of a porous titanium alloy ti6al4v with diamond structure obtained by laser power bed fusion (Lpbf). Materials 13 (22), 1–21. https://doi.org/10.3390/ma13225138.
Fedorov, A., et al., 2012. 3D slicer as an image computing platform for the quantitative imaging network. Magn. Reson. Imaging 30 (9), 1323–1341. https://doi.org/10.1016/j.mri.2012.05.001.
Finazzi, V., et al., Jan. 2019. Design rules for producing cardiovascular stents by selective laser melting: geometrical constraints and opportunities. Procedia Struct. Integr. 15, 16–23. https://doi.org/10.1016/j.prostr.2019.07.004.
Finazzi, V., Demir, A.G., Biffi, C.A., Migliavacca, F., Petrini, L., Previtali, B., Jul. 2020. Design and functional testing of a novel balloon-expandable cardiovascular stent in CoCr alloy produced by selective laser melting. J. Manuf. Process. 55, 161–173. https://doi.org/10.1016/j.jmapro.2020.03.060.
Fragoudakis, R., Karditsas, S., Savaidis, G., Michailidis, N., 2014. The effect of heat and surface treatment on the fatigue behaviour of 56SiCr7 spring steel,". Jan. In: Procedia Engineering, 74, pp. 309–312. https://doi.org/10.1016/j.proeng.2014.06.268.
GraphPad Software Inc., "GraphPad." San Diego, California, United States.
Guerra, A.J., Ciurana, J., Jan. 2018. 3D-printed bioabsorbable polycaprolactone stent: the effect of process parameters on its physical features. Mater. Des. 137, 430–437. https://doi.org/10.1016/j.matdes.2017.10.045.
Gunning, P.S., Vaughan, T.J., McNamara, L.M., 2014. Simulation of self expanding transcatheter aortic valve in a realistic aortic root: implications of deployment geometry on leaflet deformation, 1989–2001, Sep Ann. Biomed. Eng. 42 (9). https://doi.org/10.1007/s10439-014-1051-3.
Holzer, R., Hijazi, Z., Nov. 2008. The off-versus on-label use of medical devices in interventional cardiovascular medicine?: clarifying the ambiguity between regulatory labeling and clinical decision making, part III: structural heart disease interventions. Cathet. Cardiovasc. Interv. 72 (6), 848–852. https://doi.org/10.1002/ccd.21708.
ISO - ISO 4288:1996 - Geometrical Product Specifications (GPS) — Surface Texture: Profile Method — Rules and Procedures for the Assessment of Surface Texture." .
Jermihov, P.N., Jia, L., Sacks, M.S., Gorman, R.C., Gorman, J.H., Chandran, K.B., Mar. 2011. Effect of geometry on the leaflet stresses in simulated models of congenital bicuspid aortic valves. Cardiovasc. Eng. Technol. 2 (1), 48–56. https://doi.org/10.1007/s13239-011-0035-9.
Jiménez, J.M., Davies, P.F., 2009. Hemodynamically driven stent strut design. Aug Ann. Biomed. Eng. 37 (8), 1483–1494. https://doi.org/10.1007/s10439-009-9719-9.
Kasparek, M.F., et al., May 2019. Dual-energy CT and ceramic or titanium prostheses material reduce CT artifacts and provide superior image quality of total knee arthroplasty. Knee Surg. Sports Traumatol. Arthrosc. 27 (5), 1552–1561. https://doi.org/10.1007/s00167-018-5001-8.
Kenny, D.P., Hijazi, Z.M., Mar. 2017. Current status and future potential of transcatheter interventions in congenital heart disease. Circ. Res. 120, 1015–1026. https://doi.org/10.1161/CIRCRESAHA.116.309185, 6. Lippincott Williams and Wilkins.
Kornowski, R., Hong, M.K., Tio, F.O., Bramwell, O., Wu, H., Leon, M.B., Jan. 1998. In-stent restenosis: contributions of inflammatory responses and arterial injury to neointimal hyperplasia. J. Am. Coll. Cardiol. 31 (1), 224–230. https://doi.org/10.1016/S0735-1097(97)00450-6.
Lally, C., Dolan, F., Prendergast, P.J., 2005. Cardiovascular stent design and vessel stresses: a finite element analysis. J. Biomech. 38 (8), 1574–1581, Aug. https://doi.org/10.1016/j.jbiomech.2004.07.022.
Lally, C., Kelly, D.J., Prendergast, P.J., Stents, 2006. in Wiley Encyclopedia of Biomedical Engineering. Hoboken, NJ, USA. John Wiley & Sons, Inc.
Lee Ventola, C., Oct. 2014. Medical applications for 3D printing: current and projected uses. P T 39 (10), 704–711.
Lhuissier, P., de Formanoir, C., Martin, G., Dendievel, R., Godet, S., Nov. 2016. Geometrical control of lattice structures produced by EBM through chemical etching: investigations at the scale of individual struts. Mater. Des. 110, 485–493. https://doi.org/10.1016/j.matdes.2016.08.029.
Li, H., Qiu, T., Zhu, B., Wu, J., Wang, X., 2013. Design optimization of coronary stent based on finite element models. Sci. World J., 630243 https://doi.org/10.1155/2013/630243, 2013.
Maleki, E., Bagherifard, S., Bandini, M., Guagliano, M., Jan. 2021. Surface post-treatments for metal additive manufacturing: progress, challenges, and opportunities. Addit. Manuf. 37, 101619 https://doi.org/10.1016/j.addma.2020.101619. Elsevier B.V.
Marsden, A.L., Feinstein, J.A., Jan. 2015. Computational modeling and engineering in pediatric and congenital heart disease. Curr. Opin. Pediatr. 27 (5), 587–596. https://doi.org/10.1097/MOP.0000000000000269. Lippincott Williams and Wilkins.
Materialise NV, "Magics 23.02." (Leuven, Belgium).
McClean, D.R., Eigler, N.L., 2002. Stent design: implications for restenosis. Rev. Cardiovasc. Med. 3 (Suppl. 5).
McGee, O.M., Gunning, P.S., McNamara, A., McNamara, L.M., Aug. 2018. The impact of implantation depth of the Lotus$^{TM}$ valve on mechanical stress in close proximity to the bundle of His. Biomech. Model. Mechanobiol. https://doi.org/10.1007/s10237-018-1069-9.
McKenna, C.G., Vaughan, T.J., Mar. 2021. A finite element investigation on design parameters of bare and polymer-covered self-expanding wire braided stents. J. Mech. Behav. Biomed. Mater. 115, 104305 https://doi.org/10.1016/j.jmbbm.2020.104305.
Misra, S.K., et al., Jun. 2017. 3D-Printed multidrug-eluting stent from graphene-nanoplatelet-doped biodegradable polymer composite. Adv. Healthc. Mater. 6 (11), 1700008 https://doi.org/10.1002/adhm.201700008.
DMG Mori, "RDesigner" Bielefeld, (Germany).
DMG Mori, "ROperator" Bielefeld, Germany.
Murphy, B.P., Savage, P., McHugh, P.E., Quinn, D.F., 2003. The stress-strain behavior of coronary stent struts is size dependent. Ann. Biomed. Eng. 31 (6), 686–691. https://doi.org/10.1114/1.1569268.
Ngo, T.D., Kashani, A., Imbalzano, G., Nguyen, K.T.Q., Hui, D., Jun. 2018. Additive manufacturing (3D printing): a review of materials, methods, applications and challenges. Compos. B Eng. 143, 172–196. https://doi.org/10.1016/j.compositesb.2018.02.012. Elsevier Ltd.
Niinomi, M., Akahori, T., 2010. Improvement of the fatigue life of titanium alloys for biomedical devices through microstructural control. Expet Rev. Med. Dev. 7 (4), 481–488. https://doi.org/10.1586/erd.10.16. Expert Reviews Ltd.
Persenot, T., Buffiere, J.Y., Maire, E., Dendievel, R., Martin, G., Jan. 2017. Fatigue properties of EBM as-built and chemically etched thin parts. Procedia Struct. Integr. 7, 158–165. https://doi.org/10.1016/j.prostr.2017.11.073.
Qiu, T.Y., Song, M., Zhao, L.G., May 2018. A computational study of crimping and expansion of bioresorbable polymeric stents. Mech. Time-Dependent Mater. 22 (2), 273–290. https://doi.org/10.1007/s11043-017-9371-y.
Rocatello, G., De Santis, G., De Bock, S., De Beule, M., Segers, P., Mortier, P., Sep. 2019. Optimization of a transcatheter heart valve frame using patient-specific computer simulation. Cardiovasc. Eng. Technol. 10 (3), 456–468. https://doi.org/10.1007/s13239-019-00420-7.
Shibbani, K., Kenny, D., McElhinney, D., Hijazi, Z.M., Moran, T., Jun. 2016. Identifying gaps in technology for congenital interventions: analysis of a needs survey from congenital interventional cardiologists. Pediatr. Cardiol. 37 (5), 925–931. https://doi.org/10.1007/s00246-016-1372-0.
Sing, S.L., Huang, S., Yeong, W.Y., 2020. Effect of solution heat treatment on microstructure and mechanical properties of laser powder bed fusion produced cobalt-28chromium-6molybdenum. Jan Mater. Sci. Eng. A 769, 138511. https://doi.org/10.1016/j.msea.2019.138511.
Taylor, C.A., Figueroa, C.A., Aug. 2009. Patient-specific modeling of cardiovascular mechanics. Annu. Rev. Biomed. Eng. 11 (1), 109–134. https://doi.org/10.1146/annurev.bioeng.10.061807.160521.
Van Hooreweder, B., Lietaert, K., Neirinck, B., Lippiatt, N., Wevers, M., Jun. 2017. CoCr F75 scaffolds produced by additive manufacturing: influence of chemical etching on powder removal and mechanical performance. J. Mech. Behav. Biomed. Mater. 70, 60–67. https://doi.org/10.1016/j.jmbbm.2017.03.017.
van Lith, R., et al., 2016. 3D-Printing strong high-resolution antioxidant bioresorbable vascular stents. Adv. Mater. Technol. 1 (9), 1600138 https://doi.org/10.1002/admt.201600138.
Vossoughi, J., Vaishnav, R.N., Patel, D.J., 1982. ANISOTROPY OF THE AORTIC TISSUE IN THE AXIAL AND TRANSVERSE DIRECTIONS. Jan., pp. 179–182. https://doi.org/10.1016/b978-0-08-028826-0.50042-1
Vrancken, B., Thijs, L., Kruth, J.P., Van Humbeeck, J., Nov. 2012. Heat treatment of Ti6Al4V produced by selective laser melting: microstructure and mechanical properties. J. Alloys Compd. 541, 177–185. https://doi.org/10.1016/j.jallcom.2012.07.022.
Wen, P., et al., Oct. 2018. Laser additive manufacturing of Zn metal parts for biodegradable applications: processing, formation quality and mechanical properties. Mater. Des. 155, 36–45. https://doi.org/10.1016/j.matdes.2018.05.057.
Zahedmanesh, H., John Kelly, D., Lally, C., 2010. Simulation of a balloon expandable stent in a realistic coronary artery-Determination of the optimum modelling strategy. J. Biomech. 43 (11), 2126–2132, Aug. https://doi.org/10.1016/j.jbiomech.2010.03.050.
Zhao, H.Q., Nikanorov, A., Virmani, R., Jones, R., Pacheco, E., Schwartz, L.B., Jul. 2009. Late stent expansion and neointimal proliferation of oversized nitinol stents in peripheral arteries. Cardiovasc. Intervent. Radiol. 32 (4), 720–726. https://doi.org/10.1007/s00270-009-9601-z.